

Method of the Particle-in-Cell Simulation for the Y-point in the Pulsar Magnetosphere

Mitsuhiro UMIZAKI

Graduate School of Science and Engineering, Yamagata University

1-4-12 Kojirakawa, Yamagata 990-8560

mumizaki@ksirius.kj.yamagata-u.ac.jp

and

Shinpei SHIBATA

Department of Physics, Yamagata University

1-4-12 Kojirakawa, Yamagata 990-8560

shibata@ksirius.kj.yamagata-u.ac.jp

(Received 2009 October 9; accepted 2009 November 27)

Abstract

Recent observations in X-ray and Gamma-ray suggest that the emission region of the pulsar magnetosphere can be multifold. In particular, the open-close boundary of the magnetic field, so-called the Y-point, can be the place where magnetic field energy converts into the plasma heat and/or flow energy. Here, we present a new Particle-in-Cell code in axisymmetric geometry, which can be applied to the Y-point of the pulsar magnetosphere. The electromagnetic solver is used in the two-dimensional grid points with the cylindrical coordinate (R, z), while the particle solver operates in the three-dimensional Cartesian coordinate (x, y, z) by use of Buneman-Boris method. The particle motion can be relativistic. The inner boundary conditions are set up to generate rotation of the magnetosphere in use of the force-free semi-analytic solution given by Uzdensky (2003, ApJ, 598, 446).

The code has been verified by dispersion relations of all the wave modes in an electron-positron plasma.

The initial test run is also presented to demonstrate the Y-shaped structure at the top of the dead zone on the light cylinder. We suggest that the structure is variable with quasi-periodicity with magnetic reconnection and that plasma will be accelerated and/or heated. In the time-averaged point of view, break up of the ideal-MHD condition takes place in the vicinity of the Y-point.

Key words: magnetic fields — MHD — pulsars: general — stars: neutron

1. Introduction

Recently many authors have intensively studied the magnetosphere of the rotation powered pulsars by means of computer simulations in force-free approximation (Contopoulos et al. 1999; Mckinney 2006; Timokhin 2006; Spitkovsky 2006), magneto-hydrodynamics (MHD) (Komissarov 2006; Bucciantini et al. 2006), two component MHD (Kojima & Oogi 2009) and particle simulation (Wada & Shibata 2007). In such studies, boundary layers, e.g. the equatorial current sheet and the surface of the star, are sometimes troublesome. Dissipation is suggested in the boundary layers (Komissarov 2006), but it can be numerical. Acceleration and heating likely take place in the magnetic neutral sheet around the equatorial plane. The inner edge of the neutral sheet, which is called the “Y-point”, is the open-close boundary of the magnetic field structure (figure 1). Location of the Y-point is not certain and can be inside of the light cylinder (Uzdensky 2003).

In this paper, we study the Y-point in microscopic point of view to understand the dissipative process in the boundary layer. We expect that our simulation provides a hint for the appropriate boundary conditions for the global simulation. As has been suggested by Lyubarskii (1996), another possibility is that the Y-point might be a gamma-ray source. Pulsed gamma-ray radiation is previously attributed to the outer gaps and/or the polar caps. One may say that the radiation near and beyond the light cylinder becomes DC components, but this may not be the case. Recently, Kirk et al. (2002) proposed that the magnetic neutral sheet in the wind far from the light cylinder can be the source of the gamma-ray pulses. If dissipation of the magnetic field around the Y-point takes place, radiation from the vicinity of the Y-point would also contribute to the pulsed high energy emission.

Uzdensky (2003) calculated the force-free solution around the Y-point. However, he found that the force-free condition is broken around the neutral sheet. The global MHD simulation (Komissarov 2006) also suggested breakdown of force-free condition around the neutral sheet and the magnetic energy conversion to the thermal and kinetic energy. The plasma inertia and magnetic dissipation seem to play an important role around the Y-point.

We intend to study the Y-point via newly developed axisymmetric particle-in-cell (PIC) method in the cylindrical coordinates. This paper is aimed to establish the numerical code, the results of code check, and the initialization for the Y-point simulation. Some of the initial result shall be given though detailed analysis shall be given in a subsequent paper. In our scheme, the system is reflection symmetry with respect to the equator, which is the lower boundary. The free boundary condition is imposed on the outer boundary, which should be continued to the wind zone. The left and upper boundaries (inner boundaries) are assumed to satisfy the force-free solution given by Uzdensky (2003).

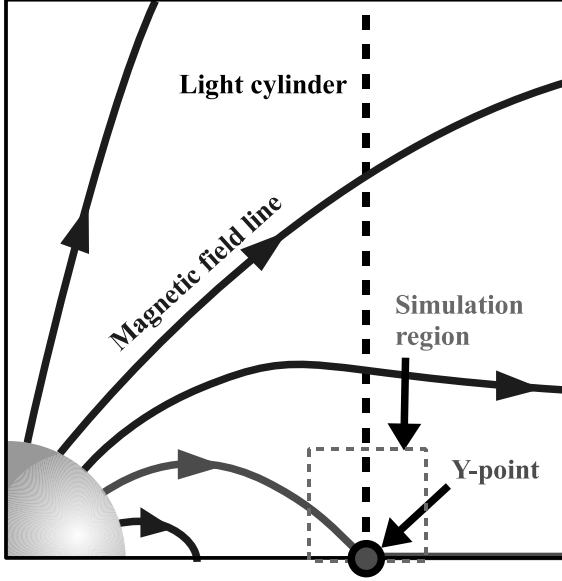


Fig. 1. The meridional plane of the pulsar magnetosphere.

2. Particle-in-Cell Code

Both particle code and Vlasov code describe the plasma kinetic effect. However, Vlasov simulation requires huge computer memory, so that we use the particle code in our simulation. The simplest system to treat the Y-point would be the axisymmetric one, and therefore we developed axisymmetric PIC code using cylindrical coordinates.

2.1. Particle motion solver

We use Buneman-Boris method in Cartesian coordinates. Then, particles are distributed in the three-dimensional Cartesian coordinates (x, y, z) and solved by Buneman-Boris method. Therefore, if a suitable inner boundary condition of \mathbf{E} and \mathbf{B} are given, particles rotate around the z -axis in the 3D space. Afterwards, we transform the particle coordinates to the cylindrical ones (R, φ, z) and solve the field quantities in the R - z plane.

The relativistic equation of motion is

$$\frac{d\mathbf{u}}{dt} = \frac{q}{m} \left[\mathbf{E} + \frac{1}{c\gamma} \mathbf{u} \times \mathbf{B} \right], \quad (1)$$

where \mathbf{u} is the space part of the four-velocity, q is the charge, m is the rest mass, γ is the Lorentz factor, and \mathbf{E} and \mathbf{B} are the electric and the magnetic fields, respectively. In Cartesian coordinate, \mathbf{E} and \mathbf{B} are given by

$$\mathbf{E} = (E_R \cos \varphi - E_\varphi \sin \varphi, E_R \sin \varphi + E_\varphi \cos \varphi, E_z), \quad (2)$$

$$\mathbf{B} = (B_R \cos \varphi - B_\varphi \sin \varphi, B_R \sin \varphi + B_\varphi \cos \varphi, B_z). \quad (3)$$

Equation (1) is rewritten in a centered-difference form as follows

$$\frac{\mathbf{u}^{n+1/2} - \mathbf{u}^{n-1/2}}{\Delta t} = \frac{q}{m} \left(\mathbf{E}^n + \frac{\mathbf{u}^{n+1/2} + \mathbf{u}^{n-1/2}}{2c\gamma} \times \mathbf{B}^n \right), \quad (4)$$

where n and Δt are the number and increment of the time steps.

Buneman-Boris method divides equation (4) into three steps.

1st step : an acceleration by \mathbf{E} for $\Delta t/2$

$$\mathbf{u}^- = \mathbf{u}^{n-1/2} + \frac{q}{m} \mathbf{E}^n \frac{\Delta t}{2}. \quad (5)$$

2nd step : a rotation by \mathbf{B} for Δt

$$\mathbf{u}^0 = \mathbf{u}^- + \mathbf{u}^- \times \mathbf{T}, \quad (6)$$

$$\mathbf{u}^+ = \mathbf{u}^- + \frac{2}{1 + T^2} \mathbf{u}^0 \times \mathbf{T}, \quad (7)$$

where $\mathbf{T} = q\mathbf{B}^n \Delta t / (2mc\gamma^-)$ and $\gamma^- = \sqrt{1 + (u^-/c)^2}$.

3rd step : an acceleration by \mathbf{E} for $\Delta t/2$

$$\mathbf{u}^{n+1/2} = \mathbf{u}^+ + \frac{q}{m} \mathbf{E}^n \frac{\Delta t}{2}. \quad (8)$$

Finally, $\mathbf{v}^{n+1/2}$ is calculated as follows,

$$\mathbf{v}^{n+1/2} = \mathbf{u}^{n+1/2} / \sqrt{1 + (u^{n+1/2}/c)^2}. \quad (9)$$

The position of the particles is updated by

$$\mathbf{x}^{n+1} = \mathbf{x}^{n+1/2} + \mathbf{v}^{n+1/2} \frac{\Delta t}{2}. \quad (10)$$

2.2. Electromagnetic field solver

Maxwell equations are solved in the cylindrical coordinates with axisymmetry by the Leap-Frog method. The magnetic field is updated by the Faraday's law,

$$\frac{\partial \mathbf{B}}{\partial t} = -c \nabla \times \mathbf{E} \quad (11)$$

and the electric field is updated by the Ampère's law,

$$\frac{\partial \mathbf{E}}{\partial t} = -4\pi \mathbf{J} + c \nabla \times \mathbf{B}, \quad (12)$$

where \mathbf{J} is the current density.

2.2.1. Field definition

In the R - z plane, fields are defined as shown in figure 2, with indices j and k for R and z coordinates, respectively. For example, the φ -components of \mathbf{E} , \mathbf{B} and \mathbf{J} are given at $(R_{j+1/2}, z_{k+1/2})$, but the R -components are given at $(R_{j+1/2}, z_k)$.

2.2.2. Update of magnetic field

We update the magnetic field by $\Delta t/2$ using the Faraday's law,

$$\frac{\partial B_R}{\partial t} = c \frac{\partial E_\varphi}{\partial z}, \quad (13)$$

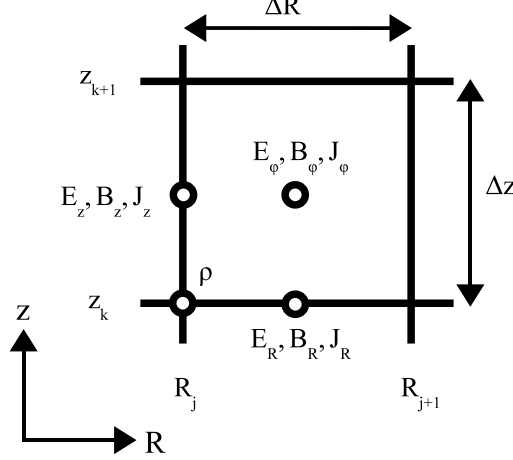


Fig. 2. Location of the grid quantities.

$$\frac{\partial B_\varphi}{\partial t} = -c \left(\frac{\partial E_R}{\partial z} - \frac{\partial E_z}{\partial R} \right), \quad (14)$$

$$\frac{\partial B_z}{\partial t} = -\frac{c}{R} \frac{\partial}{\partial R} (RE_\varphi), \quad (15)$$

which are written in centered-difference form,

$$B_{R,j+1/2,k}^n = B_{R,j+1/2,k}^{n-1/2} + c \frac{E_{\varphi,j+1/2,k+1/2}^n - E_{\varphi,j+1/2,k-1/2}^n}{\Delta z} \frac{\Delta t}{2}, \quad (16)$$

$$B_{\varphi,j+1/2,k+1/2}^n = B_{\varphi,j+1/2,k+1/2}^{n-1/2} - c \left(\frac{E_{R,j+1/2,k+1}^n - E_{R,j+1/2,k}^n}{\Delta z} - \frac{E_{z,j+1,k+1/2}^n - E_{z,j,k+1/2}^n}{\Delta R} \right) \frac{\Delta t}{2}, \quad (17)$$

$$B_{z,j,k+1/2}^n = B_{z,j,k+1/2}^{n-1/2} - \frac{c}{R_j} \frac{R_{j+1/2} E_{\varphi,j+1/2,k+1/2}^n - R_{j-1/2} E_{\varphi,j-1/2,k+1/2}^n}{\Delta R} \frac{\Delta t}{2}. \quad (18)$$

2.2.3. Update of electric field

We update the electric field by Δt using the Ampère's law,

$$\frac{\partial E_R}{\partial t} = -4\pi J_R - c \frac{\partial B_\varphi}{\partial z}, \quad (19)$$

$$\frac{\partial E_\varphi}{\partial t} = -4\pi J_\varphi + c \left(\frac{\partial B_R}{\partial z} - \frac{\partial B_z}{\partial R} \right), \quad (20)$$

$$\frac{\partial E_z}{\partial t} = -4\pi J_z + \frac{c}{R} \frac{\partial}{\partial R} (RB_\varphi), \quad (21)$$

which are rewritten in centered-difference form,

$$E_{R,j+1/2,k}^{n+1} = E_{R,j+1/2,k}^n$$

$$- \left(4\pi J_{R,j+1/2,k}^{n+1/2} + c \frac{B_{\varphi,j+1/2,k+1/2}^{n+1/2} - B_{\varphi,j+1/2,k-1/2}^{n+1/2}}{\Delta z} \right) \Delta t, \quad (22)$$

$$E_{\varphi,j+1/2,k+1/2}^{n+1} = E_{\varphi,j+1/2,k+1/2}^n + \left[-4\pi J_{\varphi,j+1/2,k+1/2}^{n+1/2} + c \left(\frac{B_{R,j+1/2,k+1}^{n+1/2} - B_{R,j+1/2,k}^{n+1/2}}{\Delta z} - \frac{B_{z,j+1,k+1/2}^{n+1/2} - B_{z,j,k+1/2}^{n+1/2}}{\Delta R} \right) \right] \Delta t, \quad (23)$$

$$E_{z,j,k+1/2}^{n+1} = E_{z,j,k+1/2}^n + \left(-4\pi J_{z,j,k+1/2}^{n+1/2} + \frac{c}{R_j} \frac{R_{j+1/2} B_{\varphi,j+1/2,k+1/2}^{n+1/2} - R_{j-1/2} B_{\varphi,j-1/2,k+1/2}^{n+1/2}}{\Delta R} \right) \Delta t. \quad (24)$$

2.3. Calculation of charge density

To obtain the charge density at (R_j, z_k) , charge of a particle is distributed to the neighboring four grids with weightings in proportion to the volumes opposite to the particle, i.e. the shaded region in figure 3 for the left-bottom grid point. We calculate thus the charge density

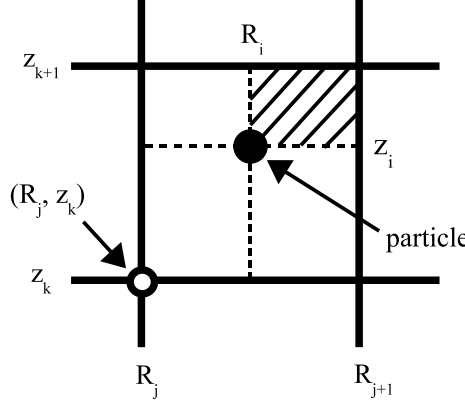


Fig. 3. Schematic diagram for interpolation between a particle and grids.

with shape factors,

$$S_j(R_i) = \begin{cases} (R_{j+1} - R_i) / \Delta R & \text{for } R_j \leq R_i < R_{j+1} \\ (R_i - R_{j-1}) / \Delta R & \text{for } R_{j-1} \leq R_i < R_j \\ 0 & \text{otherwise} \end{cases} \quad (25)$$

$$S_k(z_i) = \begin{cases} (z_{k+1} - z_i) / \Delta z & \text{for } z_k \leq z_i < z_{k+1} \\ (z_i - z_{k-1}) / \Delta z & \text{for } z_{k-1} \leq z_i < z_k \\ 0 & \text{otherwise} \end{cases} \quad (26)$$

in our code. The charge distributed to (R_j, z_k) is

$$Q_{j,k} = \sum_i q_i S_j(R_i) S_k(z_i), \quad (27)$$

which yields the charge density,

$$\rho_{j,k} = Q_{j,k}/V_{j,k}, \quad (28)$$

where $V_{j,k} = 2\pi R_j \Delta R \Delta z$.

On the other hand, the electric field at the position of the i -th particle (R_i, z_i) is given by

$$\begin{aligned} \mathbf{E}(R_i, z_i) = & S_j S_k \begin{pmatrix} (R_j/R_i) E_{R,j,k} \\ E_{\varphi,j,k} \\ E_{z,j,k} \end{pmatrix} + S_j S_{k+1} \begin{pmatrix} (R_j/R_i) E_{R,j,k+1} \\ E_{\varphi,j,k+1} \\ E_{z,j,k+1} \end{pmatrix} + \\ & S_{j+1} S_k \begin{pmatrix} (R_{j+1}/R_i) E_{R,j+1,k} \\ E_{\varphi,j+1,k} \\ E_{z,j+1,k} \end{pmatrix} + S_{j+1} S_{k+1} \begin{pmatrix} (R_{j+1}/R_i) E_{R,j+1,k+1} \\ E_{\varphi,j+1,k+1} \\ E_{z,j+1,k+1} \end{pmatrix} \end{aligned} \quad (29)$$

The magnetic field is also given in the same form.

2.4. Calculation of current density

Current density is also calculated with the shape factors:

$$\mathbf{J}_{j,k} = \sum_i q_i S_j(R_i) S_k(z_i) \mathbf{v}_i. \quad (30)$$

We interpolate the current densities at the full integer grids to those at the appropriate grid points shown in figure 2 by

$$J_{R,j+1/2,k} = \frac{R_{j+1} J_{R,j+1,k} + R_j J_{R,j,k}}{2R_{j+1/2}}, \quad (31)$$

$$J_{\varphi,j+1/2,k+1/2} = \frac{J_{\varphi,j+1,k+1} + J_{\varphi,j,k+1} + J_{\varphi,j+1,k} + J_{\varphi,j,k}}{4}, \quad (32)$$

$$J_{z,j,k+1/2} = \frac{J_{z,j,k+1} + J_{z,j,k}}{2}. \quad (33)$$

Since the above current density does not guarantee the charge conservation law, the electric fields contain an error. Therefore, we use the following procedure to correct the electric field. Gauss' law yields

$$\nabla \cdot (\mathbf{E}' + \mathbf{E}_c) = 4\pi\rho, \quad (34)$$

where \mathbf{E}' is the obtained field by (22), (23), (24) and \mathbf{E}_c is the correction. It follows from (34) that \mathbf{E}_c is obtained by

$$\nabla \cdot \mathbf{E}_c = 4\pi\rho_c, \quad (35)$$

where $\rho_c = \rho - \nabla \cdot \mathbf{E}'/4\pi$. Then, we solve

$$-\nabla^2 \phi_c = 4\pi\rho_c \quad (36)$$

and we get $\mathbf{E}_c = -\nabla\phi_c$.

2.5. A calculation of the PIC method for one time step

A calculation cycle of the PIC method is shown in figure 4. We interpolate the electromagnetic fields at the particle positions, $\mathbf{E}_i, \mathbf{B}_i$, from the values of the given grids points, $\mathbf{E}_{j,k}, \mathbf{B}_{j,k}$. We integrate the equations of motion and move the particle positions. We next calculate the charge densities and current densities using the particle data. Electromagnetic fields are updated by integrating Maxwell equations.

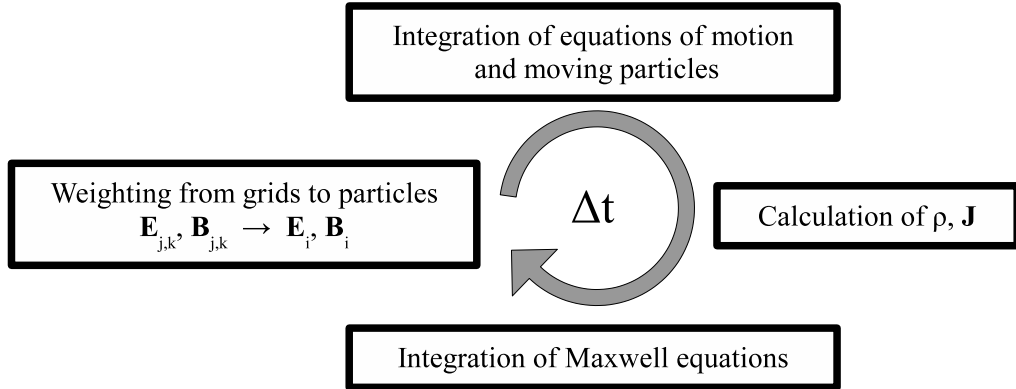


Fig. 4. A calculation cycle of the PIC method.

3. Result

3.1. Code check

In order to check the code, we obtain the dispersion relations of waves in electron-positron plasmas for Light mode, X-mode, Fast mode, O-mode, Electromagnetic mode, and Alfvén mode. The boundary conditions are perfect conductor for the outer radius and periodic for z -direction. The plasma is uniform and has no bulk velocity. Particle distribution for the thermal velocities is non-relativistic Maxwellian. The simulation settings are given in table 1.

3.1.1. Light mode

The simulation for Case A in Table 1 demonstrates the light-mode.

The linear dispersion relation of the light mode is

$$\omega^2 = \omega_p^2 + c^2 k^2, \quad (37)$$

where

$$\omega_p = \sqrt{\frac{8\pi ne^2}{m\gamma_{\text{th}}}}, \quad (38)$$

where

$$\gamma_{\text{th}} = 1 + \frac{\Gamma}{\Gamma - 1} \frac{k_B T}{mc^2}, \quad (39)$$

Γ is a ratio of specific heat, k_B is the Boltzmann constant, and T is the temperature. The

Table 1. The simulation settings for the code check. \mathbf{B}_0 is background magnetic field, v_{th} is thermal velocity, ω_p is plasma frequency, and Ω is gyro-frequency.

	Case A	Case B	Case C
\mathbf{B}_0	(0, 0, 0)	(0, B_φ , 0)	(0, 0, B_z)
v_{th}	$0.1c$	$0.1c$	$0.1c$
$\Delta R, \Delta z$	$v_{\text{th}}\omega_p^{-1}$	$v_{\text{th}}\omega_p^{-1}$	$v_{\text{th}}\omega_p^{-1}$
$\Delta t/\Delta R$	0.2	0.2	0.2
Grid number ($R \times z$)	128×512	128×512 (X, Fast) 256×512 (O)	128×512
Total time step	4096	4096	4096
Particle number per grid	200	200	200
Ω/ω_p	0	1	1

frequency of the light mode is ω_p at $k = 0$ and asymptotically it approaches to $\omega = ck$ in high wave numbers.

We compute the Fourier transform with respect to z and then integrate that in R -direction. We do not impose any kind of initial perturbation, i.e., there is only thermal noise initially. Figure 5 shows the result for B_φ , showing that dispersion relation (37) is well reproduced.

3.1.2. X-mode, Fast mode, and O-mode

We next analyze the perpendicular propagating waves. The simulation settings are given in Case B in Table 1.

The linear dispersion relations of X-mode (positive-signed) and Fast mode (negative-signed) are

$$\omega^2 = \frac{1}{2} \left[(c^2 + c_s^2)k^2 + \Omega^2 + \omega_p^2 \pm \sqrt{(c^2 - c_s^2)^2 k^4 + 2(c^2 - c_s^2)(\omega_p^2 - \Omega^2)k^2 + (\Omega^2 + \omega_p^2)^2} \right], \quad (40)$$

where

$$\Omega = \frac{eB}{mc\gamma_{\text{th}}}, \quad (41)$$

and c_s is the speed of the sonic wave,

$$c_s = \sqrt{(\Gamma - 1) \frac{\gamma_{\text{th}} - 1}{\gamma_{\text{th}}}} c. \quad (42)$$

The frequency of the X-mode becomes the upper hybrid frequency $\omega_{\text{UH}} = \sqrt{\omega_p^2 + \Omega^2}$ at $k = 0$, and asymptotically approaches $\omega = ck$ in high wave numbers. The frequency of the Fast mode is $\omega = 0$ at $k = 0$, and asymptotically approaches to $\omega = c_s k$ in high wave numbers.

Figure 6 shows Fourier transform of B_φ , showing that these waves are well fitted by the dispersion relations (40).

The linear dispersion relation of O-mode is

$$\omega^2 = \omega_p^2 + c^2 k^2. \quad (43)$$

The frequency of the O-mode is ω_p at $k = 0$, and asymptotically approaches to $\omega = ck$ for high wave numbers.

Figure 7 shows Fourier transform of B_R , showing that this wave is well fitted by the dispersion relation (43).

3.1.3. Electromagnetic mode and Alfvén mode

Finally, we analyze the parallel propagating waves, Case C, for which the simulation settings are given in Table 1.

The linear dispersion relations of the electromagnetic mode (positive-signed) and Alfvén mode (negative-signed) are

$$\omega^2 = \frac{1}{2} \left[c^2 k^2 + \omega_{\text{UH}}^2 \pm \sqrt{(c^2 k^2 + \omega_{\text{UH}}^2)^2 - 4c^2 k^2 \Omega^2} \right]. \quad (44)$$

The frequency of the electromagnetic mode is ω_{UH} at $k = 0$, and asymptotically approaches to $\omega = ck$ in high wave numbers. The frequency of the Alfvén mode is $\omega = 0$ at $k = 0$, and asymptotically approaches to the relativistic gyro-frequency in high wave numbers.

Figure 8 shows Fourier transform of B_φ , showing that these waves are well fitted by the dispersion relations (44).

3.1.4. Summary of the code check

We perform the simulations for waves in electron-positron plasmas in order to check the newly developed axisymmetric PIC code. We find that dispersion relations of Light mode, X-mode, Fast mode, O-mode, Electromagnetic mode, and Alfvén mode are well reproduced. Thus we conclude that the code is successfully constructed.

3.2. Application to the Y-point of the pulsar magnetosphere

3.2.1. Outline of the Y-point simulation

Regarding the local simulation in the global structure shown in figure 1, the boundary condition is of great importance for the simulation of the Y-point. Inner region would be well approximated by the force-free solution, so that the left and upper boundaries (inner boundaries) are assumed to be the force-free solution by Uzdensky (2003) as shown in figure 9. On the other hand, it is known that Uzdensky's solution is broken down beyond the light cylinder. It is likely that the particle inertia becomes important, and the frozen-in condition breaks down near the Y-point where the magnetic energy density decreases and plasma is more important. The outer (right-side) boundary may be crossed by super-fast wind. Then we impose free boundary for the right-side boundary. The lower boundary can be treated as reflection symmetry. The boundary conditions might be fair only if the simulation box is large enough. As for the initial condition we also use the Uzdensky's solution. The simulation shall be continued until the system becomes quasi steady state.

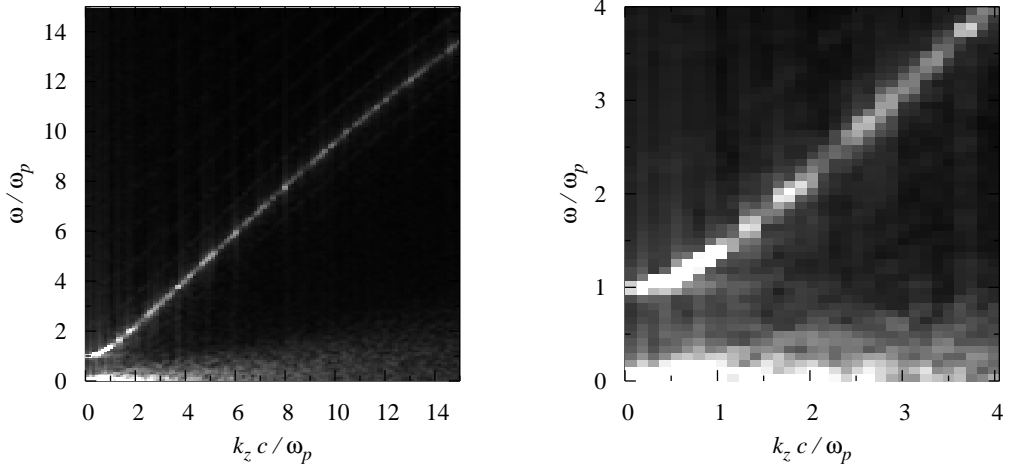


Fig. 5. The dispersion relation diagrams of the light mode. Gray map indicates Fourier transformation of B_φ . The left figure is the full simulation scale and the right is the lower frequency part.

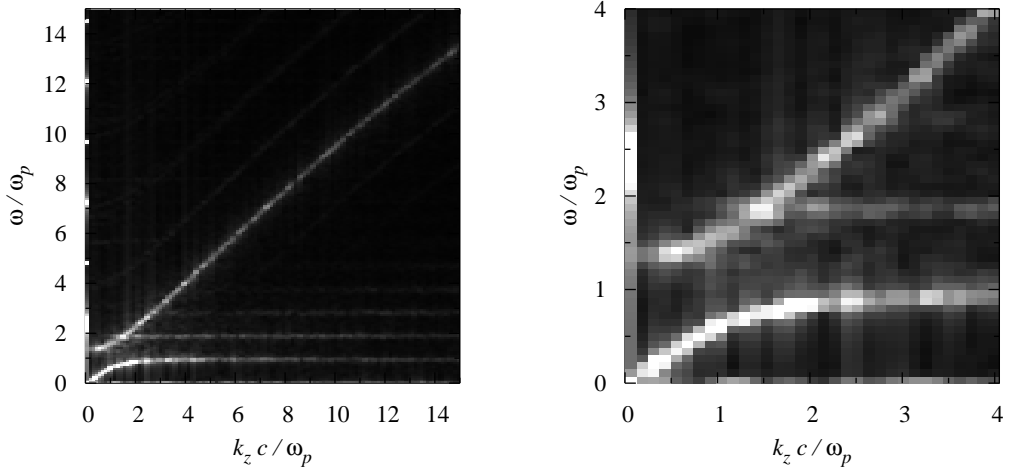


Fig. 6. Fourier transformation of B_φ . The dispersion relation diagrams of the X-mode (upper frequency wave) and the Fast mode (lower frequency wave). The left figure is the full simulation scale and the right is the lower frequency part. For this case, $\omega_{\text{UH}} = \sqrt{2}$ and $c_s \approx 6.6 \times 10^{-2}$.

3.2.2. The force-free solution around the Y-point

As shown by Uzdensky (2003), if the Y-point is located at the light cylinder, the regularity condition at the light cylinder determines the poloidal magnetic flux, Ψ , and the poloidal current, $\tilde{I}(\Psi)$. The obtained magnetic field is shown in figure 10. Once the force-free solution Ψ and $\tilde{I}(\Psi)$ are obtained, the electromagnetic field, charge density, and current density are given by

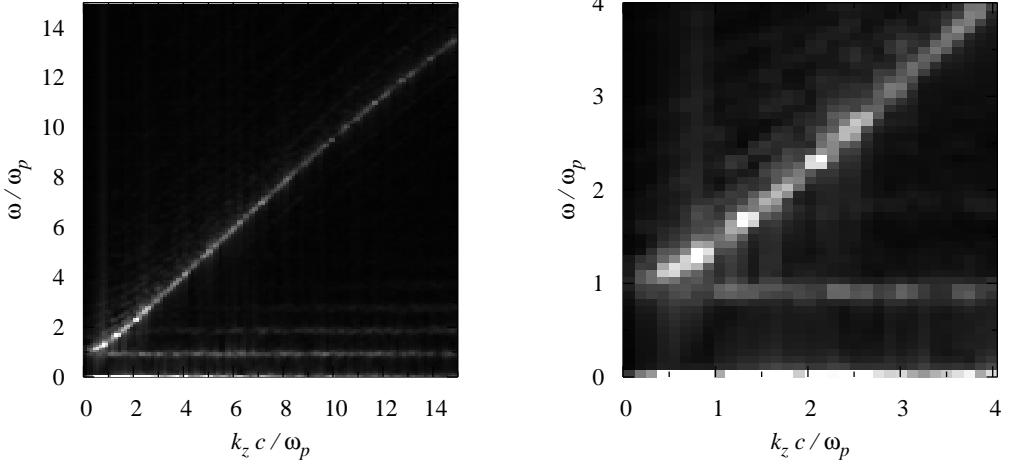


Fig. 7. Fourier transformation of B_R for Case B. The dispersion relation of the O-mode is well reproduced. The left figure is the full simulation scale and the right is the lower frequency part.

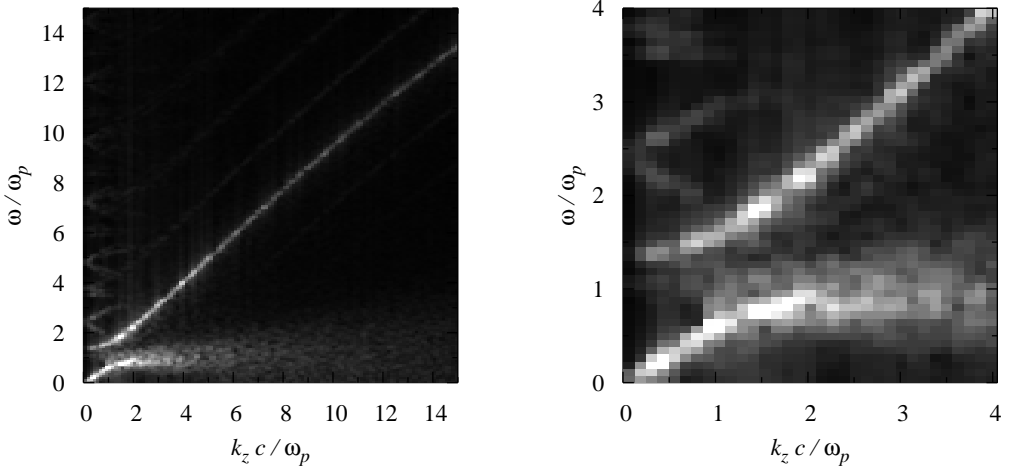


Fig. 8. Fourier transformation of B_φ for Case C. The dispersion relation of the Electromagnetic mode (upper frequency wave) and the Alfvén mode (lower frequency wave) can be seen. The left figure is the full simulation scale and the right is the lower frequency part.

$$\mathbf{B}_p = -\frac{e_\varphi}{R} \times \nabla \Psi, \quad (45)$$

$$B_\varphi = \frac{\tilde{I}}{R}, \quad (46)$$

$$\mathbf{E} = -\frac{\Omega(\Psi)}{c} \nabla \Psi, \quad (47)$$

$$\rho = \frac{1}{4\pi} \nabla \cdot \mathbf{E}, \quad (48)$$

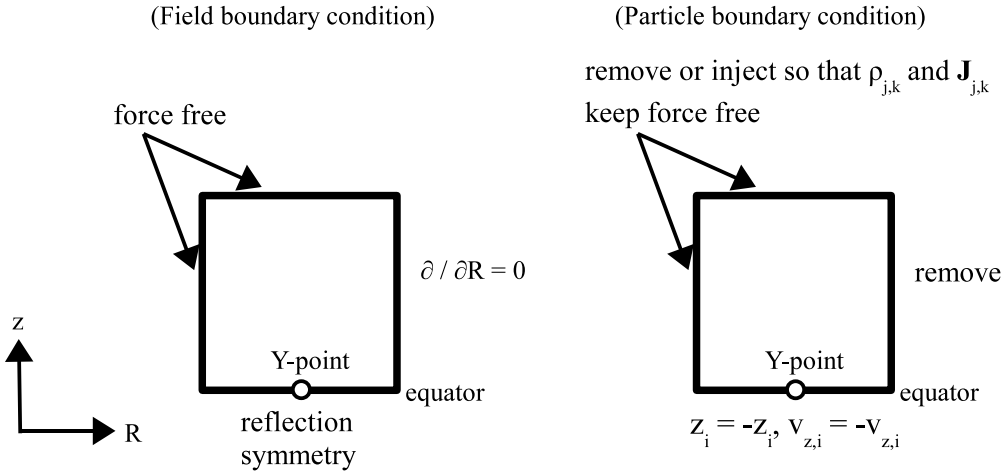


Fig. 9. The boundary conditions for the Y-point simulation.

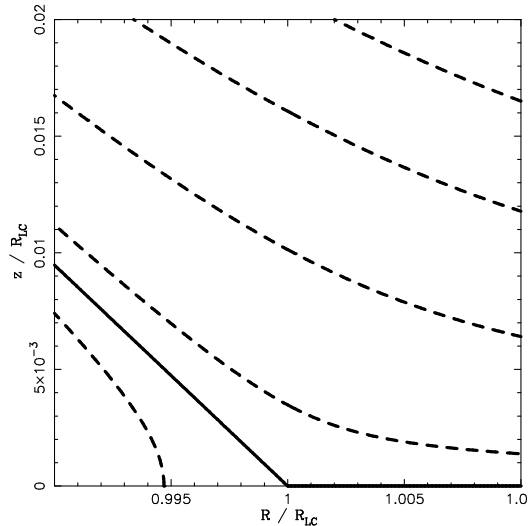


Fig. 10. The force-free solution around the Y-point given by Uzdensky (2003). The dashed lines represent poloidal magnetic field line. The solid line represents the separatrix, $\Psi = 0$, between the open and closed field-line regions.

$$\mathbf{J}_p = \frac{c}{4\pi} \frac{d\tilde{I}}{d\Psi} \mathbf{B}_p, \quad (49)$$

$$J_\varphi = -\frac{c}{4\pi R} (\nabla^2 \Psi - 2B_z), \quad (50)$$

where Ω is the angular velocity of the star.

The bulk velocities of the plasma are restricted by

$$\mathbf{v}_\pm = \boldsymbol{\Omega} \times \mathbf{r} + \kappa_\pm \mathbf{B}, \quad (51)$$

where + and - respectively indicate positron and electron, \mathbf{r} is the position vector, $\boldsymbol{\Omega}$ is the angular velocity vector, and κ is a scalar function to be determined.

Since the force-free solution does not concern about the plasma density and bulk velocity, we introduce two model parameters,

$$n = n_+ + n_- \quad (52)$$

and

$$\bar{\gamma} = \frac{1}{\sqrt{1 - (\bar{v}/c)^2}}, \quad (53)$$

where $\bar{v} = |(\gamma_+ n_+ \mathbf{v}_+ + \gamma_- n_- \mathbf{v}_-)/(\gamma_+ n_+ + \gamma_- n_-)|$. Giving the two model parameters, we obtain n_{\pm} and \mathbf{v}_{\pm} , which satisfy the force-free solution for ρ and \mathbf{J} . The $N_{j,k} = n_{\pm} V_{j,k}$ particles, whose velocity is \mathbf{v}_{\pm} , are distributed uniformly in the (j,k) -cell by a random number generator.

3.2.3. Inner boundary condition

The inner boundary conditions are imposed for the innermost and uppermost cells (figure 11). For the inner boundary cells, we assume the density, n , so that the number of particle in a cell, $N_{j,k} = n V_{j,k}$, is constant. With the force-free charge density, we have the particle numbers for each species to be distributed in each cell,

$$N_{\pm} = \frac{1}{2} \left(N_{j,k} \pm \frac{\rho}{q} V_{j,k} \right), \quad (54)$$

where we typically take $N_{j,k} = \text{constant} = 100$. The field-aligned velocity of the particles are restricted by the force-free current density, i.e.,

$$q(n_+ \kappa_+ - n_- \kappa_-) = \frac{c}{4\pi} \frac{d\tilde{I}}{d\Psi}, \quad (55)$$

where the poloidal velocities for each species are given by

$$\mathbf{v}_{p\pm} = \kappa_{\pm} \mathbf{B}_p. \quad (56)$$

The mean value of κ is given by

$$\bar{\kappa} = \frac{\gamma_+ n_+ \kappa_+ + \gamma_- n_- \kappa_-}{\gamma_+ n_+ + \gamma_- n_-} \quad (57)$$

where $\gamma_{\pm} = [1 - (v_{\pm}/c)^2]^{-1/2}$. Given $\bar{\gamma}$, (55) and (57) are the simultaneous equations with respect to κ_{\pm} . In the present simulation, we set typically $\bar{\gamma} = 50$. Thus the velocity in the boundary cells are given by (51). The current density $\mathbf{J} = q(n_+ \mathbf{v}_+ - n_- \mathbf{v}_-)$ automatically satisfies both (49) and (50).

We remove or inject particles in the innermost and uppermost cells so that ρ_{\pm} and \mathbf{J}_{\pm} keep these force-free formulae.

3.2.4. Initialization

As was mentioned before, the initial state of the plasma is set to be the Uzdensky's force-free solution. The electromagnetic field is set by (45), (46) and (47). For the particles, we defined the closed field region, i.e. the dead zone, as $\Psi > 0$ and the open field region, i.e. the wind zone, as $\Psi < 0$. In the dead zone, we take $N_{j,k} = 100$ and $\kappa_{\pm} = 0$. It is known that there

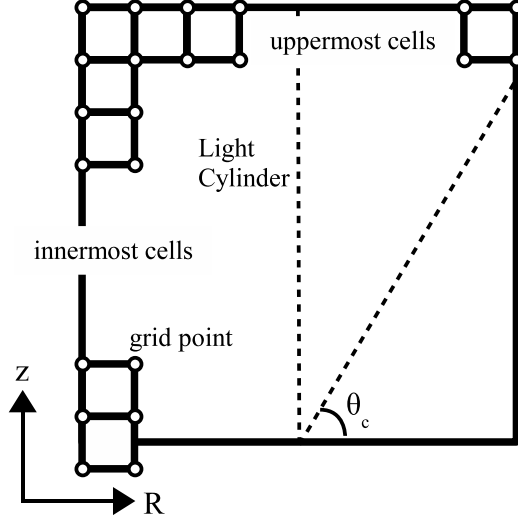


Fig. 11. The innermost cells and the uppermost cells. We imposed force-free condition for those cells. In the wedge shape region $\theta < \theta_c$, Uzdensky solution breaks down.

is a critical line shown in figure 11 with the critical angle $\theta_c \approx 62^\circ$ from the equatorial plane and that in the wedge like region $\theta < \theta_c$, we have $|\mathbf{E}| > |\mathbf{B}|$. In the force-free wind zone, we use the continuity condition, $\nabla \cdot (n_{\pm} \mathbf{v}_{\pm}) = 0$, instead of setting $N_{j,k}$, and take $\bar{\gamma} = 50$. In the non-force-free wind zone, we assume $\mathbf{v}_{p\pm} \parallel \mathbf{B}_p$ instead of using (51), and take $N_{j,k}=100$ and $\bar{\gamma} = 50$. In any case, the memory of the initial condition will be lost in a few light-transit times, so that the final state will not be affected by the initial condition.

3.2.5. Normalization

We normalize the distance, velocity, and magnetic field respectively by the light radius, $R_{LC} = c/\Omega$, the speed of light, and $(B_*/2)(R_*/R_{LC})^3$, where B_* is the field strength at the poles and R_* is the radius of the star, respectively. In order to increase computational efficiency, we renormalize distance and time by the grid spacing, Δx , and $\Delta t/2$, respectively.

Normalization constants and renormalization constants are shown in table 2.

3.3. Initial result of the Y-point simulation

We have performed a test run for the Y-point. After a time of 1/60 rotation, the plasma attains a steady state, in some sense, with quasi-periodic variability with time scale of 1/300 rotation. Figure 12 shows the poloidal magnetic field vector averaged over 1/300 rotation to indicate the formation of Y-point around the intersection of the light cylinder and the equatorial plane. In a short time scales, however, we see that some part of the closed field line at the top of the dead zone is broken to make a magnetic island with magnetic reconnection, and the island go outward. However, sometimes such a island can come back and merge with the dead zone. Basically, plasma flows out across the outer (right) boundary. However, the plasma near the equator move out and in quasi-periodically. In the run, magnetic reconnection is

Table 2. The normalization constants and renormalization constants.

	Normalization constants	Renormalization constants
distance	$x_0 = R_{LC}$	$x_{00} = \Delta x$
time	$t_0 = R_{LC}/c$	$t_{00} = \Delta t/2$
velocity	$v_0 = c$	$v_{00} = \Delta x/(\Delta t/2)$
electromagnetic field	$B_0 = (B_*/2)(R_*/R_{LC})^3$	$B_{00} = \Delta x^{-1/2}/(\Delta t/2)$
charge density	$\rho_0 = B_0 R_{LC}^{-1}$	$\rho_{00} = \Delta x^{-3/2}/(\Delta t/2)$
current density	$J_0 = B_0 R_{LC}^{-1} c$	$J_{00} = \Delta x^{-1/2}(\Delta t/2)^{-2}$
charge	$q_0 = B_0 R_{LC}^2$	$q_{00} = \Delta x^{3/2}/(\Delta t/2)$
mass	$m_0 = B_0^2 R_{LC}^3 c^{-2}$	$m_{00} = 1$

essential, and the associated heating and acceleration should be important. Figure 13 shows the ratio, $|\mathbf{E}|/|\mathbf{B}|$, averaged over the same period. The region where $|\mathbf{E}| > |\mathbf{B}|$ degenerates near the equatorial plane. It is suggested that the electric-field-dominant region becomes several Debye length in thickness. With the initial run, we suggest that the Y-point can be active in magnetic field dissipation associated by magnetic reconnection. The electric-field-dominant region ($|\mathbf{E}| > |\mathbf{B}|$), which is suggested by the force-free solution, shrinks into a thin equatorial sheet.

In a subsequent paper, we study the acceleration and heating, namely the conversion of magnetic energy into plasma quantitatively.

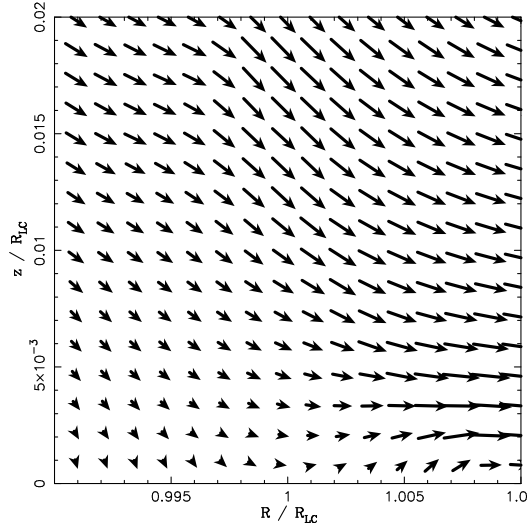


Fig. 12. The vector of the averaged poloidal magnetic field around the Y-point.

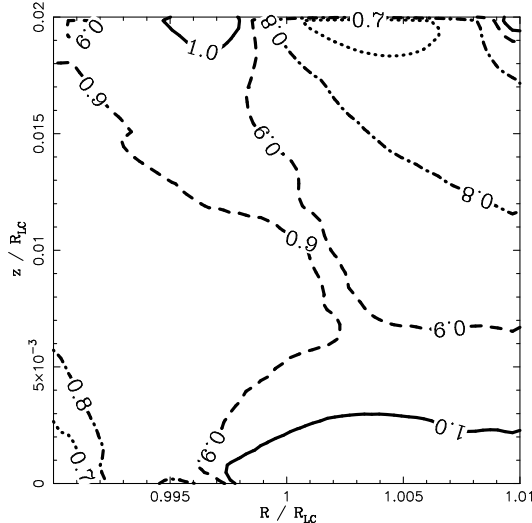


Fig. 13. The $|E|/|B|$ distribution around the Y-point.

4. Summary

We develop the axisymmetric PIC code in order to analyze the Y-point in the pulsar magnetosphere. The code is verified by the dispersion relations of waves in electron-positron plasmas. We also established the appropriate boundary conditions for the Y-point in use of the force-free semi-analytic solution. We have performed a test run and find that the Y-point is actually formed at the top of the dead zone on the light cylinder. It is, however, variable with magnetic reconnection. We suggest that the Y-point can be a region around which the magnetic field energy convert into the plasma heat and outflow and subsequently into radiation. We also suggest that some plasma jet can be flow back to polar cap region to produce radio emission. In the next step, we will perform large scale simulations and analyze the Y-point structure in detail.

Numerical computations were in part carried out on NEC SX-9 at Center for Computational Astrophysics, CfCA, of National Astronomical Observatory of Japan and in part carried out on PRIMEPOWER 850 at Networking and Computing Service Center of Yamagata University. This work was supported in part by a Grant-in-Aid from the Ministry of Education, Science, Sports and Culture of Japan (19540235). The page charge of this paper is supported by CfCA.

References

Birdsall, C. K., & Langdon, A. B. 1985, Plasma Physics via Computer Simulation (McGraw-Hill, New York)
 Bucciantini, N., Thompson, T. A., Arons, J., Quataert, E., & Del Zanna, L. 2006, MNRAS, 368,

Contopoulos, I., Kazanas, D., & Fendt, C. 1999, *ApJ*, 511, 351-358

Kirk, J. G., Skjæraasen, O., & Gallant, Y. 2002, *A&A*, 388, L29-L32

Kojima, Y., & Oogi, J. 2009, *MNRAS*, 398, 271-279

Komissarov, S. S. 2006, *MNRAS*, 367, 19-31

Lyubarskii, Y. E. 1996, *A&A*, 311, 172-178

Matsumoto, H., & Omura, Y. 1993, in *Computer Space Plasma Physics*, ed. H. Matsumoto, Y. Omura (Terra Scientific Pub, Tokyo) 21

McKinney, J. C. 2006, *MNRAS*, 368, L30-L34

Spitkovsky, A. 2006, *ApJ*, 648, L51-L54

Timokhin, A. N. 2006, *MNRAS*, 368, 1055-1072

Uzdensky, D. A. 2003, *ApJ*, 598, 446-457

Wada, T., & Shibata, S. 2007, *MNRAS*, 376, 1460-1464